RSC Advances

PAPER

View Article Online
View Journal | View Issue

Cite this: *RSC Adv.*, 2018, **8**, 2338

Activation of peroxymonosulfate by metal (Fe, Mn, Cu and Ni) doping ordered mesoporous Co_3O_4 for the degradation of enrofloxacin

Jing Deng, Chen Ya, Yongjian Ge, Yongqing Cheng, Yijing Chen, Mengyuan Xu and Hongyu Wang *

Received 16th July 2017
Accepted 2nd January 2018

DOI: 10.1039/c7ra07841b

rsc.li/rsc-advances

Various transition metals (Fe, Mn, Cu and Ni) were doped into ordered mesoporous Co_3O_4 to synthesize Co_3O_4-composite spinels. Their formation was evidenced by transmission electronic microscopy (TEM), X-ray diffraction (XRD) and Brunauer–Emmett–Teller (BET) analysis. It was found that Co_3O_4-composite spinels could efficiently activate peroxymonosulfate (PMS) to remove enrofloxacin (ENR) and the catalytic activity followed the order Co_3O_4–$CuCo_2O_4$ > Co_3O_4–$CoMn_2O_4$ > Co_3O_4–$CoFe_2O_4$ > Co_3O_4–$NiCo_2O_4$. Moreover, through the calculation of the specific apparent rate constant (k_{sapp}), it can be proved that the Co and Cu ions had the best synergistic effect for PMS activation. The Co_3O_4-composite spinels presented a wide pH range for the activation of PMS, but strong acidic and alkaline conditions were detrimental to ENR removal. Higher reaction temperature could promote the PMS activation process. Sulfate radical was identified as the dominating reactive species in Co_3O_4-composite spinel/PMS systems through radical quenching experiments. Meanwhile, the probable mechanisms concerning Co_3O_4-composite spinel activated PMS were proposed.

1. Introduction

During the past years, sulfate radical ($SO_4^{-\bullet}$) based advanced oxidation processes (SR-AOPs) have attracted an increasing interest among researchers owing to their great potential in degradation or even mineralization of recalcitrant organic pollutants.[1] Compared with the hydroxyl radical ($^{\bullet}OH$), $SO_4^{-\bullet}$ possesses a longer lifespan, higher independence of pH and higher selectivity of oxidation.[2,3] Peroxymonosulfate (PMS), a precursor of $SO_4^{-\bullet}$, is deemed as a cost-effective and environmental-friendly oxidant.[4] PMS remains stable in aqueous solution and barely decomposes into $SO_4^{-\bullet}$ by itself, but it can be activated to produce $SO_4^{-\bullet}$ by the use of UV, transition metals, and some nonmetal catalysts.[5–7] Among different activation technologies, transition metals have attracted much attention due to their lower energy consumption and higher activation efficiency. Actually, many transition metal ions such as Co^{2+}, Mn^{2+}, Ni^{2+}, Fe^{2+}, Ru^{3+}, Ce^{3+} and so forth, have been proved as qualified catalysts for PMS activation.[2] Of note, Co^{2+} has been found to possess the highest reactivity.[8] Unfortunately, the Co^{2+}/PMS process is unfavorable in practical application because of the toxicity of Co^{2+}.

In order to relieve the secondary pollution, heterogeneous cobalt-based catalysts have become a research hotspot. Anipsitakis *et al.* firstly employed Co_3O_4 to activate PMS and found Co_3O_4 presented an excellent catalytic behavior in the activation of PMS.[9] Chen *et al.* successfully prepared nanoscale Co_3O_4 and tested its catalytic performance in PMS solution, results showed that 0.2 mM acid orange 7 (AO7) can be completely degraded within 30 min by 2 mM PMS in the presence of 0.5 g L^{-1} Co_3O_4.[10] Pu *et al.* fabricated three types of Co_3O_4 using different metal organic frameworks, and found that all the Co_3O_4 exhibited outstanding catalytic activity and the difference in catalytic ability can be attributed to the difference in specific surface area.[11] Consequently, Co_3O_4/PMS system is quite acceptable from the view of application due to the high activation efficiency and limitation of cobalt leaching. However, on the basis of the underlying threat of cobalt ions, it is essential to take measures to further limit the cobalt leakage during PMS activation.

It is reported that bimetallic oxides may be desirable catalysts to ease the conflict between catalytic performance and metal ions leaching, because intimate interactions between two metals can effectively suppress the leakage of metal ions, such as Fe–Co interactions in $CoFe_2O_4$.[2] Moreover, bimetallic oxides are also prominent PMS activators. Su *et al.* synthesized a series of $Co_xFe_{3-x}O_4$ nanoparticles and found that the higher cobalt content in $Co_xFe_{3-x}O_4$ showed the higher catalytic activity towards PMS.[12] The high catalytic behavior of $CoFe_2O_4$ was also illustrated in our previous study.[13] Yao *et al.* reported that $CoMn_2O_4$ showed stronger catalytic activity than Co_3O_4, Mn_2O_3 and their physical mixture due to the synergistic effects of Co

College of Civil Engineering and Architecture, Zhejiang University of Technology, 18 Chaowang Road, Xiacheng District, Hangzhou 310014, China. E-mail: hywangzjut@163.com; Fax: +86 571 88320180; Tel: +86 571 88320180

and Mn species.[14] Similarly, $CuCo_2O_4$ also exhibited high catalytic performance and low metal leachability in PMS solution.[15] In our previous research, order mesoporous Co_3O_4 (OM-Co_3O_4) was fabricated and showed superior catalytic ability toward PMS than its spinel counterpart, but the leakage of cobalt was up to 77.74 μg L^{-1} which was higher than conventional Co_3O_4 nanoparticles.[16] Therefore, it can be reasonably speculated that cobalt leaching will reduce if some transition metals are doped to OM-Co_3O_4 to form mixed spinels with cobalt.

Herein, diverse transition metals (*i.e.*, Fe, Mn, Cu and Ni) was introduced into OM-Co_3O_4 to synthesized a series of Co_3O_4-composite spinels which were characterized by transmission electronic microscope (TEM), X-ray diffraction (XRD), Brunauer–Emmett–Teller (BET) and Zeta potential analysis. Due to the ubiquitous detection in aquatic environment,[17] enrofloxacin (ENR) was selected as target pollutant in this study. The catalytic activities of as-prepared Co_3O_4-composite spinels were systematically compared through apparent rate constant, PMS consumption, intensity of electron paramagnetic resonance (EPR) signal and specific apparent rate constant. Moreover, the effects of initial pH and reaction temperature during PMS activation were also investigated. Finally, a possible mechanism of PMS activation was proposed through quenching tests. To be best of our knowledge, it is the first time to apply order mesoporous Co_3O_4-composite spinels as effective PMS activators for the control of organic pollutants.

2. Materials and methods

2.1 Chemicals

ENR, acetonitrile (HPLC grade), Oxone (KHSO5·0.5KHSO4·0.5K2SO4, PMS, KHSO5 ≥ 47%) and 5,5-dimethyl-1-pyrroline-*N*-oxide (DMPO) were obtained from Aladdin Biochemical Technology Co., Ltd. (Shanghai, China). The silica templates KIT-6 were purchased from Nanjing XFNANO Materials Tech Co., Ltd. (Jiangsu, China). Other chemical reagents were purchased from Sinopharm Chemical Reagent Co., Ltd. (Shanghai, China). Deionized water (18 MΩ cm) was produced from an Ulupure water purification system (Shanghai, China).

2.2 Catalysts preparation and characterization

OM-Co_3O_4 was synthesized using nanocasting route with KIT-6 as hard template, and the procedure was conducted as described before.[16] For the preparation of Co_3O_4-composite spinels, 1.0 g OM-Co_3O_4 was dispersed in 2.5 mL ethanol of $Fe(NO_3)_3\cdot 9H_2O$, $Mn(NO_3)_2\cdot 4H_2O$, $Cu(NO_3)_2\cdot 3H_2O$ and $Ni(NO_3)_2\cdot 6H_2O$, respectively, and Co/M molar ratio was controlled at 3. After magnetic stirring for 1 h, the mixture was dried overnight at 60 °C and then calcined at 450 °C for 5 h (the heating rate was set at 2 °C min^{-1}). Finally, the obtained composite spinels were referenced as Co_3O_4–CoM_2O_4 (M = Fe, Mn) and Co_3O_4–MCo_2O_4 (M = Cu, Ni) which depended on the oxidation state of dopant.

The crystal structures of catalysts were characterized by X'Pert PRO diffractometer (PANalytical, Holland) with Cu Kα radiation. The morphologies and structures of Co_3O_4-composite spinels were observed using transmission electron microscopy (TEM) (Philips, Holland). N_2 adsorption and desorption isotherms were measured using ASAP 2010 analyzer (Micromeritics, USA) at liquid nitrogen temperature (−196 °C). The pH at point of zero charge (pH_{pzc}) was determined by Zetasizer Nano analyzer (Malvern, UK).

2.3 Catalytic experimental procedure

The catalytic degradation experiments were performed with a 100 mL ENR solution at 10 mg L^{-1} in 250 mL brown glass bottles, which were installed in a controlled temperature water bath stirring apparatus. In a typical run, specific amount of catalysts was added to ENR solution to receive adsorption–desorption equilibrium, followed by pH adjustment with H_2SO_4 and NaOH solution (100 mM) to ensure a desirable pH value after PMS addition. Subsequently, an appropriate amount of PMS was charged into the reaction solution to initiate experiment. At defined time intervals, 1 mL samples were collected and quenched by 0.1 mL Na_2SO_3 (100 mM). The resulting mixtures were immediately filtered by a 0.22 μm syringe filter for further analysis. All experiments were carried out in duplicates and the mean values were reported (with error bar).

2.4 Analytical methods

ENR concentrations were measured through a high-performance liquid chromatograph (HPLC, Agilent 1200, USA) with an Eclipse XDB-C18 column (5 μm particle, 150 × 4.5 mm), the concentrations were measured at $\lambda = 278$ nm using a mobile phase consisting of a mixture of acetonitrile and phosphoric acid (pH = 2.5) (v/v = 20 : 80) at a flow rate of 1.0 mL min^{-1}. The PMS concentrations were measured by the method of Waclawek *et al.*[18] EPR analysis were performed on a Bruker A300 spectrometer (Germany) with DMPO as a spin-trapping agent. The parameters of EPR spectrometer were center field was 3360.67 G, sweep width was 100 G, static field was 3310.66 G, microwave frequency was 9.42 GHz, microwave power was 2.03 mW, modulation amplitude was 1.0 G and sweep time was 30.72 s.

3. Results and discussion

3.1 Characterization

The crystalline phases of OM-Co_3O_4 and Co_3O_4-composite spinels were displayed in Fig. 1. It was worth noting that the precursors and OM-Co_3O_4 would result in the formation of composite spinels at high temperature. The lattice of Co_3O_4 would host other cations through the replacement of cobalt cations.[19] However, no significant difference can be observed between OM-Co_3O_4 and Co_3O_4-composite spinels in Fig. 1. The well-defined diffraction peaks of 2θ = 19.00°, 31.27°, 36.85°, 38.54°, 44.81°, 55.66°, 59.36° and 65.24° were corresponded to (111), (220), (311), (222), (400), (422), (511) and (440), respectively. This might be ascribed to that the unit cell parameters of $CoFe_2O_4$, $CoMn_2O_4$, $CuCo_2O_4$ and $NiCo_2O_4$ were very close to that of Co_3O_4,[19] thus these phases cannot be distinguished through XRD analysis. But according to Debye–Scherrer equation, the calculated mean crystallite sizes of OM-Co_3O_4, Co_3O_4–

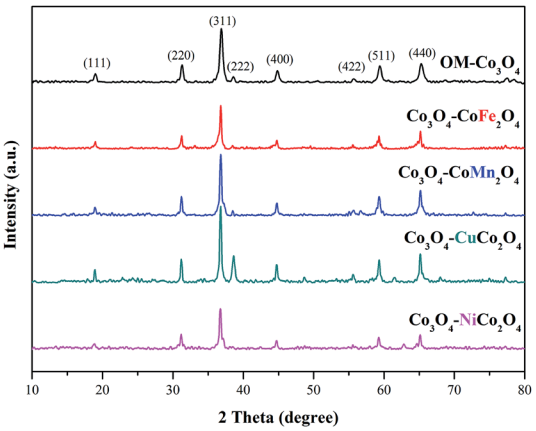

Fig. 1 XRD patterns of OM-Co_3O_4 and Co_3O_4-composite spinels.

$CoFe_2O_4$, Co_3O_4–$CoMn_2O_4$, Co_3O_4–$CuCo_2O_4$ and Co_3O_4–$NiCo_2O_4$ were 17.43, 25.32, 22.87, 27.35 and 24.86 nm, respectively. Compared with OM-Co_3O_4, the increase of mean crystallite sizes in Co_3O_4-composite spinels indicated that the introduction of metal dopants destroyed original structure of OM-Co_3O_4.

The TEM and HR-TEM images of OM-Co_3O_4 and Co_3O_4-composite spinels were showed in Fig. 2. It can be clearly seen that OM-Co_3O_4 showed a highly ordered mesoporous structure, and the spacing distances between two fringes are 0.285 and 0.467 nm, which were in conformity with (220) and (111) planes, respectively. Obviously, after the introduction of metal dopants, ordered mesoporous structure was partly or completely destroyed, which may be attributed to the formation of Co_3O_4-composite spinels. The lattice fringes can be clearly observed in HR-TEM images, indicating that highly crystalline nature of Co_3O_4-composite spinels, which was corresponded to the strong and sharp diffraction peaks in XRD analysis. Similarly with OM-Co_3O_4, the spacing distances between two fringes in Co_3O_4–$CoFe_2O_4$ were 0.281 and 0.471 nm, corresponding to (220) and (111) planes, respectively. And that in Co_3O_4–$CoMn_2O_4$ were 0.279 and 0.469 nm, which were also assigned to (220) and (111) planes, respectively. However, as for Co_3O_4–$CuCo_2O_4$ and Co_3O_4–$NiCo_2O_4$, the (111) plane was not observed, and the lattice spacing of 0.275 and 0.286 nm was corresponded to (220) plane.

The surface areas and pore size distributions of OM-Co_3O_4 and composite materials were investigated by N_2 adsorption–desorption isotherms. As shown in Fig. 3(a), all materials showed type IV isotherms, and the specific surface areas of OM-Co_3O_4, Co_3O_4–$CoFe_2O_4$, Co_3O_4–$CoMn_2O_4$, Co_3O_4–$CuCo_2O_4$ and Co_3O_4–$NiCo_2O_4$ were 66.91, 52.34, 50.92, 30.39 and 29.53 $m^2 g^{-1}$, respectively. The reduction of specific surface areas in Co_3O_4-composite spinels was ascribed to the deterioration of ordered mesoporous structure after the impregnation of metal cations, which was in accordance with the observation of TEM images. Moreover, compared with Co_3O_4–$CoFe_2O_4$ and Co_3O_4–$CoMn_2O_4$, the more significant decrease of specific surface areas in Co_3O_4–$CuCo_2O_4$ and Co_3O_4–$NiCo_2O_4$ may be related to the oxidation state of the doped metal ions. The formation of Co_3O_4–MCo_2O_4 consumed more Co_3O_4 than Co_3O_4–CoM_2O_4,[19] thus the deterioration of ordered mesoporous structure in Co_3O_4–MCo_2O_4 was more significant than that of Co_3O_4–

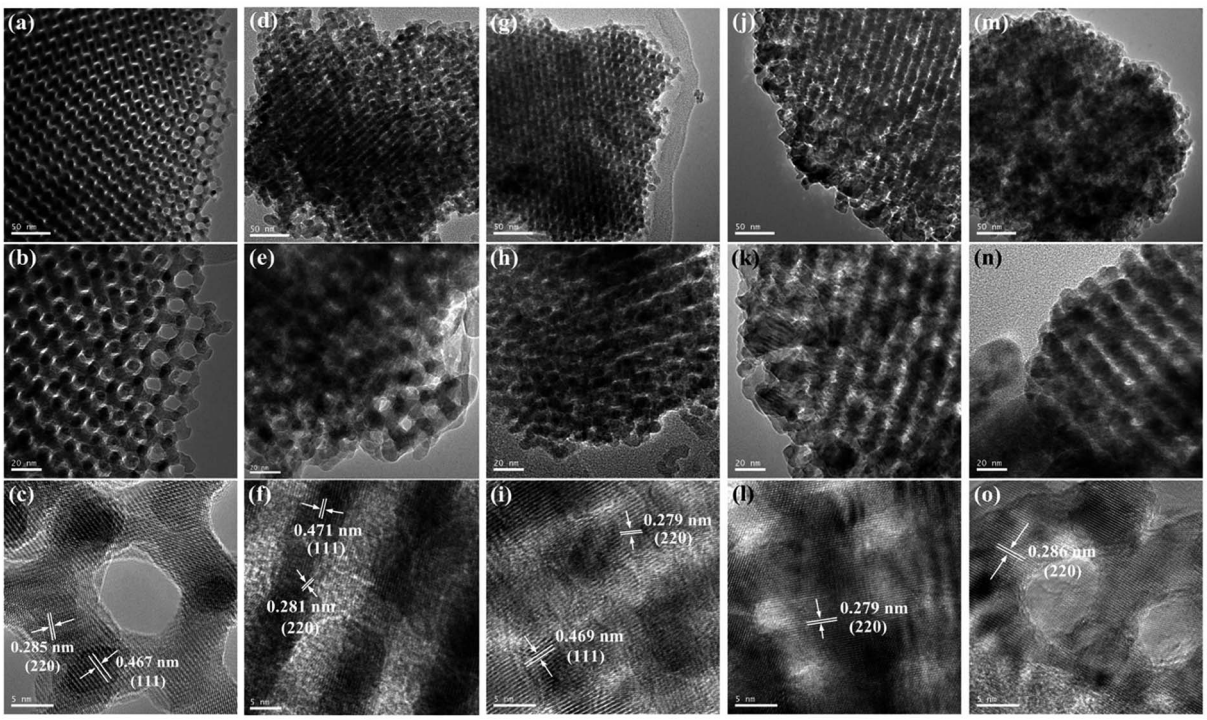

Fig. 2 TEM and HR-TEM images of OM-Co_3O_4 and Co_3O_4-composite spinels. (a)–(c) OM-Co_3O_4; (d)–(f) Co_3O_4–$CoFe_2O_4$; (g)–(i) Co_3O_4–$CoMn_2O_4$; (j)–(l) Co_3O_4–$CuCo_2O_4$; (m)–(o) Co_3O_4–$NiCo_2O_4$.

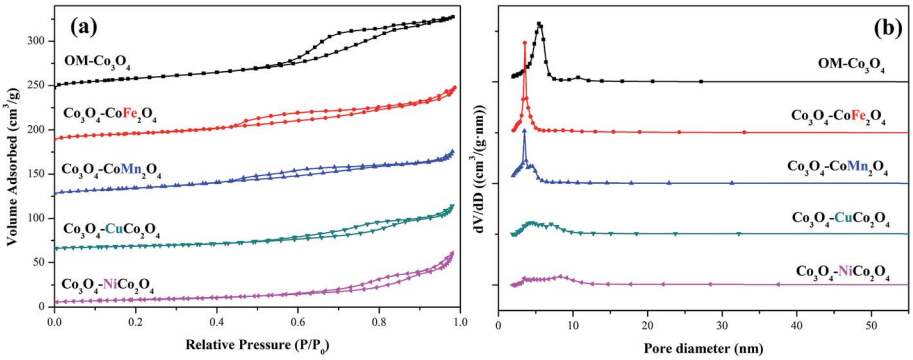

Fig. 3 (a) Nitrogen adsorption–desorption isotherms of OM-Co_3O_4 and Co_3O_4-composite spinels and (b) their pore size distributions.

CoM_2O_4, which can also be observed from TEM images. The changes of pore volume and pore diameter also demonstrated the conclusion, as seen in the Fig. 3(b), the pore volume and pore diameter all followed the order of OM-Co_3O_4 > Co_3O_4–CoM_2O_4 > Co_3O_4–MCo_2O_4. The textural parameters of OM-Co_3O_4 and Co_3O_4-composite spinels were summarized in Table 1.

XPS analysis can be used to determine the surface composition and chemical oxidation states of OM-Co_3O_4 and Co_3O_4-composite spinels. In XPS spectra of OM-Co_3O_4 (Fig. 4(a)), the sharp peak emerged at 779.6 eV was assignable to Co $2p_{3/2}$, which could be deconvoluted into octahedral Co^{3+} at 779.4 eV and tetrahedral Co^{2+} at 780.7 eV.[20] The proportions of Co^{2+} and Co^{3+} were determined to be 63.01% and 36.99%, respectively. The O 1s envelope (Fig. 4(b)) could be deconvoluted into two parts, namely the lattice oxygen (O_{latt}) at 529.2 eV and surface adsorbed oxygen (O_{ads}) at 530.8 eV.[16] Based on this deconvolution, the proportions of O_{latt} and O_{ads} were found to be 50.86% and 49.14%, respectively. After the doping of iron into OM-Co_3O_4, the content of Co^{2+} increased from 63.01% to 65.34%, which could be ascribed to the substitution of Co^{3+} with Fe^{3+} in OM-Co_3O_4. It was worth noting that the content of O_{ads} increased from 50.86% to 51.74%, which was conductive to the PMS activation.[4] As seen in Fig. 4(c), the doped iron existed in the form of positive trivalent.

3.2 Catalytic activity of Co_3O_4-composite spinels

ENR removal in different systems was presented in Fig. 5(a). Adsorption tests showed that all the catalysts exerted a low efficiency in ENR adsorption, and the highest efficiency was received by Co_3O_4–$CoFe_2O_4$ with 3.22% of ENR adsorption within 30 min, which may be attributed to the largest specific surface area. Although PMS is a strong oxidizing agent with oxidation potential of 1.82 V,[21] only 16.36% ENR could be removed by PMS in the absence of activator. However, the ENR degradation was greatly enhanced in the presence of both Co_3O_4-composite spinels and PMS. ENR can be completely removed in Co_3O_4–$CuCo_2O_4$/PMS and Co_3O_4–$CoMn_2O_4$/PMS systems, and the removal efficiencies were 96.37% and 94.56%, respectively. Furthermore, the ENR degradation well followed a pseudo-first-order kinetics pattern:

$$\ln\left(\frac{[ENR]}{[ENR]_0}\right) = -k_{app}t \quad (1)$$

where $[ENR]_0$ is the initial ENR concentration, [ENR] is the concentration of ENR at time t, and k_{app} is the apparent rate constant. As seen in Fig. 4(b), the fitting k_{app} for Co_3O_4–$CoFe_2O_4$, Co_3O_4–$CoMn_2O_4$, Co_3O_4–$CuCo_2O_4$ and Co_3O_4–$NiCo_2O_4$ are 0.122, 0.255, 0.273 and 0.097 min^{-1}, respectively, which illustrated that the catalytic activity abided by the order of Co_3O_4–$CuCo_2O_4$ > Co_3O_4–$CoMn_2O_4$ > Co_3O_4–$CoFe_2O_4$ > Co_3O_4–$NiCo_2O_4$. In addition, Fig. 4(b) provided the PMS consumption during ENR oxidation. It can be seen that Co_3O_4–$CuCo_2O_4$ consumed the maximum PMS concentration (0.4 mM), which was 1.05, 1.74 and 2.00 times higher than Co_3O_4–$CoMn_2O_4$, Co_3O_4–$CoFe_2O_4$ and Co_3O_4–$NiCo_2O_4$, respectively. This result was also confirmed the sequence of catalytic activity of Co_3O_4-composite spinels.

EPR experiments were also performed for the comparison of the catalytic activity of Co_3O_4-composite spinels. As presented

Table 1 Physicochemical properties of OM-Co_3O_4 and Co_3O_4-composite spinels

	XRD	N_2 adsorption–desorption			
Samples	Crystallite size (nm)	Surface area (m^2 g^{-1})	Pore volume (cm^3 g^{-1})	Pore diameter (nm)	pH_{pzc}
OM-Co_3O_4	17.43	66.91	0.135	8.08	5.85
Co_3O_4–$CoFe_2O_4$	25.32	52.34	0.105	7.19	4.21
Co_3O_4–$CoMn_2O_4$	22.87	50.92	0.094	6.32	3.93
Co_3O_4–$CuCo_2O_4$	27.35	30.39	0.083	5.91	4.76
Co_3O_4–$NiCo_2O_4$	24.86	29.53	0.086	6.21	5.37

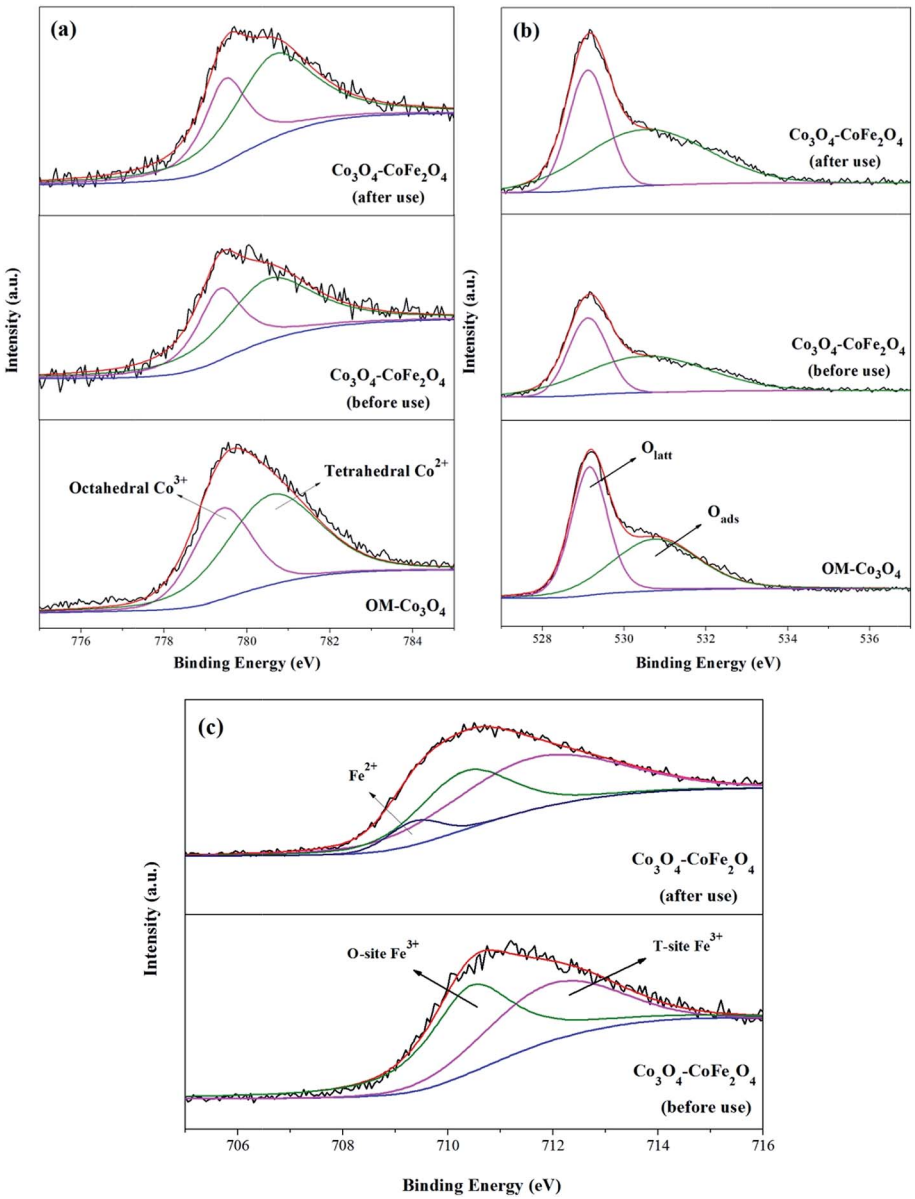

Fig. 4 XPS survey spectrum of Co $2p_{3/2}$ (a), O 1s (b) and Fe $2p_{3/2}$ (c) for OM-Co_3O_4 and Co_3O_4–$CoFe_2O_4$.

in EPR spectra (Fig. 5(c)), there was no distinctive EPR signal obtained by PMS alone. Nevertheless, simultaneous use of Co_3O_4-composite spinels and PMS could lead to obvious EPR signals. These EPR signals indicated the formation of 5,5-dimethyl-2-oxo-pyrroline-1-oxyl (DMPOX),[22,23] which was ascribed to the fast activation of PMS and efficient oxidation of DMPO,[24] also proofing the high catalytic performance of Co_3O_4-composite spinels. In addition, the signals of DMPOX caused by Co_3O_4–$CuCo_2O_4$/PMS and Co_3O_4–$CoMn_2O_4$/PMS systems were stronger than that caused by Co_3O_4–$CoFe_2O_4$ or Co_3O_4–$NiCo_2O_4$ activated PMS system (Fig. 5(b)), further authenticating the order of catalytic activity of Co_3O_4-composite spinels.

It was suggested that the catalytic performance of Co_3O_4-composite spinels not only depended on the specific surface area, but relied on dopant itself. In order to eliminate the difference in the specific surface area, the specific apparent rate constant k_{sapp} which defined as the ratio of k_{app} to the BET surface area was introduced:

$$k_{sapp} = \frac{k_{app}}{S_{BET}} \quad (2)$$

where k_{sapp} is the specific apparent rate constant, and S_{BET} is the specific surface area of composite spinels. As shown in Fig. 5(b), the k_{sapp} of Co_3O_4–$CuCo_2O_4$ (8.983×10^{-3} g (m^2 min^{-1})) was still the highest one which was 3.85, 1.79, 2.73 times higher than that of Co_3O_4–$CoFe_2O_4$, Co_3O_4–$CoMn_2O_4$ and Co_3O_4–$NiCo_2O_4$, respectively, indicating that Co and Cu ions possessed the best synergistic effect for PMS activation.

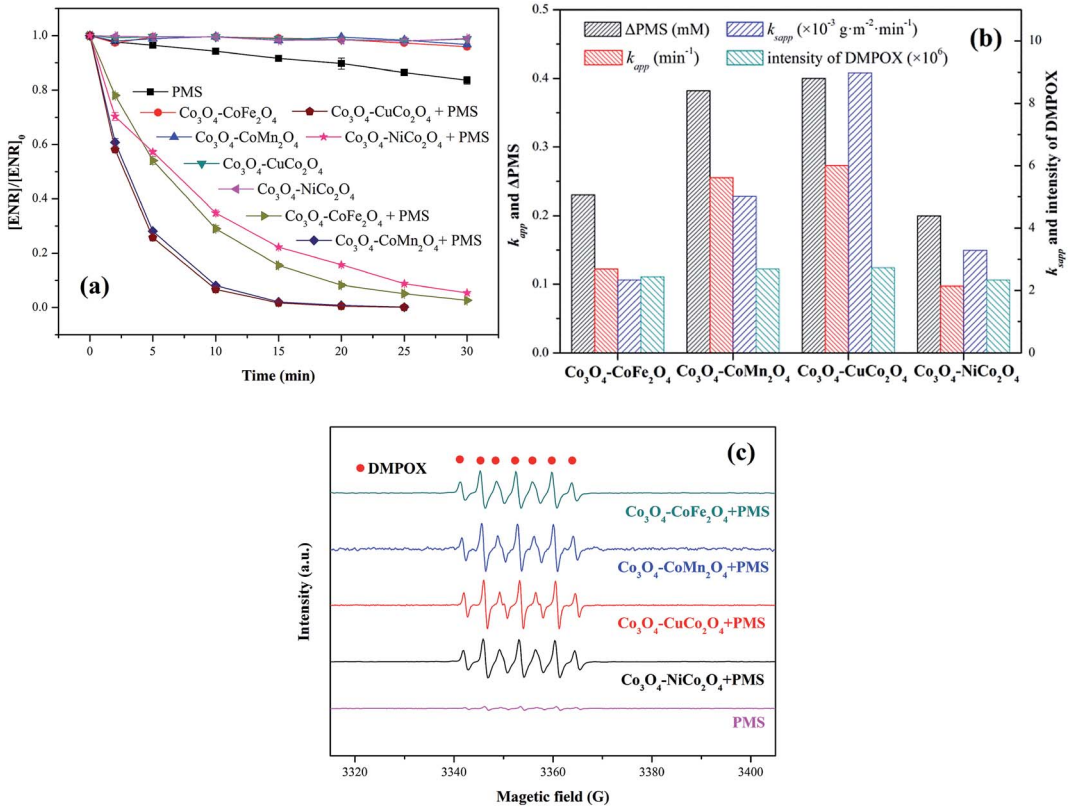

Fig. 5 (a) ENR degradation in different systems; (b) values involved in different Co_3O_4-composite spinels/PMS systems; (c) EPR spectra in different composite spinels/PMS systems (DMPO = 25 mM). Experimental condition: [ENR] = 10 mg L^{-1}, [catalyst] = 0.1 g L^{-1}, [PMS] = 1 mM, pH_0 = 6, T = 25 °C.

3.3 Effect of initial pH

The influence of initial pH ranging from 3 to 11 on ENR degradation was investigated in the PMS activation process, and the results were displayed in Fig. 6. From Fig. 6(a)–(e), it can be seen that four Co_3O_4-composite spinels all showed a wide pH range for PMS oxidation and higher ENR removals were obtained in pH range of 5 to 9 while lower removals occurred at strong acidic and alkaline conditions. Similar results were also reported by the previous investigations, such as degradation of orange II in $MnFe_2O_4$/PMS process and removal of acetaminophen in Fe_3O_4/PMS system.[25,26] The ENR degradation was significantly inhibited at strong acidic condition might be originated from the attachment of H^+ to the peroxide bond (O–O) of PMS (eqn (3)) and the change of catalyst surface charge (eqn (4)), so that the interfacial repulsion would result in a weaker catalytic performance.[27] The retardation of ENR removal at strong alkaline condition can be ascribed to the following reasons: (1) the increase of catalyst surface negative charges. The pH_{pzc} of Co_3O_4–$CoFe_2O_4$, Co_3O_4–$CoMn_2O_4$, Co_3O_4–$CoCo_2O_4$ and Co_3O_4–$NiCo_2O_4$ was 4.21, 3.93, 4.76 and 5.37, respectively (Table 1). The surface charges of catalysts were negative when solution pH was higher than pH_{pzc}. Higher solution pH would cause higher amount of negative charges on catalyst surface, which could enhance the electrostatic repulsion between catalyst surface and PMS anions. Consequently, the catalytic performance decreased at strong alkaline condition. (2) The transform of dominant PMS species. Given that pK_{a1} of H_2SO_5 was less than 0 and pK_{a2} was 9.4, SO_5^{2-} would replace HSO_5^- and become dominant PMS species when solution pH was higher than 9.4. Compared with HSO_5^- ($E^0(HSO_5^-/SO_4^{2-})$ = 1.75 V), SO_5^{2-} ($E^0(SO_5^{2-}/SO_4^{2-})$ = 1.22 V) was less oxidative and more difficult to react.[28] Additionally, SO_5^{2-} could also lead to a stronger electrostatic repulsion between catalyst surface and PMS anions.

$$SO_2 - O - O - H + H^+ \rightarrow SO_2 - O - O - H_2^+ \quad (3)$$

$$[Cat - OH] + H^+ \leftrightarrow [Cat - OH_2^+] \quad (4)$$

The values of k_{sapp} were also calculated and the results were presented in Fig. 6(f). It could be more intuitionistic to compare the catalytic performances of four Co_3O_4-composite spinels in different conditions due to the elimination of difference in specific surface area. As shown in Fig. 5(f), Co_3O_4–$CuCo_2O_4$ maintained the highest k_{sapp} values with pH varied from 3 to 11, suggesting that Co and Cu species were the best combination for PMS activation among these four spinels. However, it should be noted that the lowest k_{sapp} value was showed by Co_3O_4–$CoMn_2O_4$ at pH 11 other than Co_3O_4–$CoFe_2O_4$ or Co_3O_4–$NiCo_2O_4$. This might be closely related to pH_{pzc} of catalysts, the

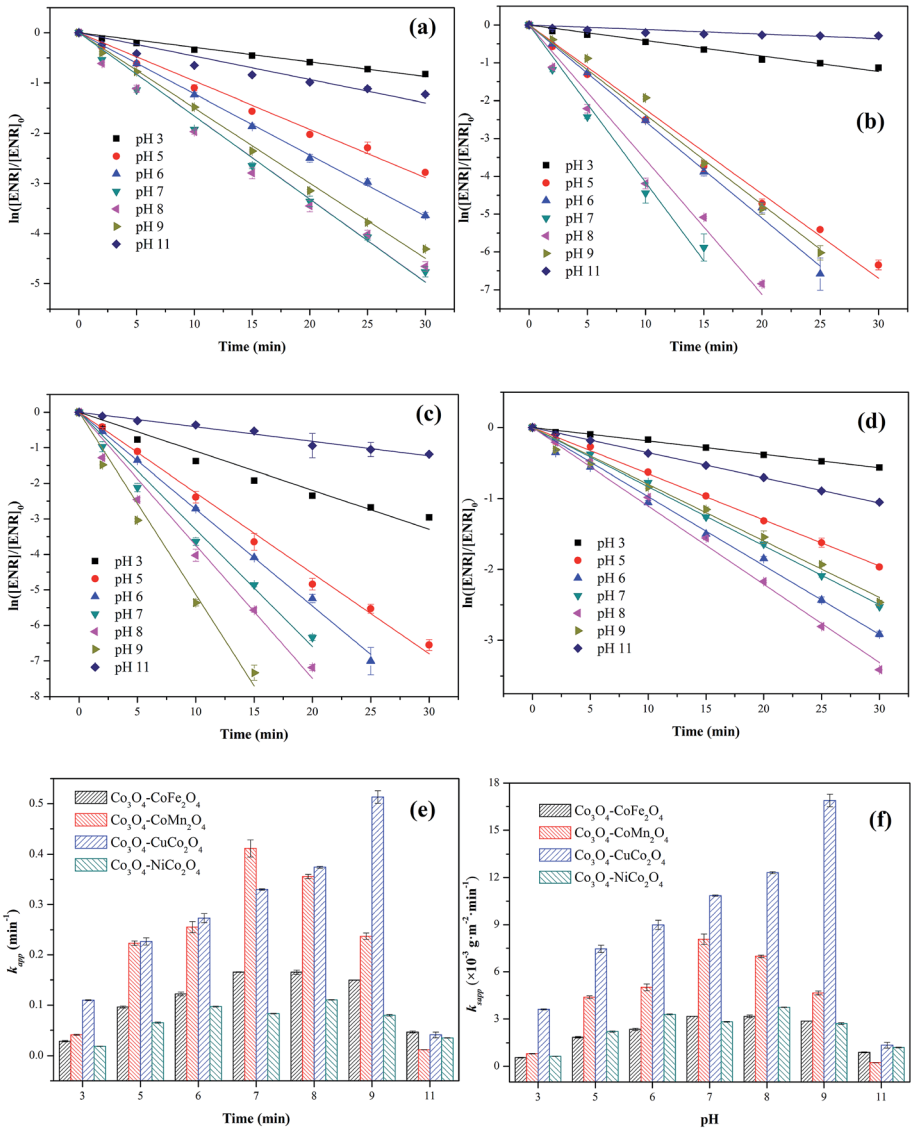

Fig. 6 Effect of initial pH on ENR degradation in different Co_3O_4-composite spinels/PMS systems: (a) Co_3O_4–$CoFe_2O_4$; (b) Co_3O_4–$CoMn_2O_4$; (c) Co_3O_4–$CuCo_2O_4$; (d) Co_3O_4–$NiCo_2O_4$. Values involved in different pH and Co_3O_4-composite spinels/PMS systems: (e) k_{app}; (f) k_{sapp}. Experimental condition: [ENR] = 10 mg L^{-1}, [catalyst] = 0.1 g L^{-1}, [PMS] = 1 mM, T = 25 °C.

pH_{pzc} of Co_3O_4–$CoMn_2O_4$ was 3.93 which was much lower than that of other three Co_3O_4-composite spinels. It manifested that Co_3O_4–$CoMn_2O_4$ could present lower performance at strong alkaline condition than others, thus Co_3O_4–$CoMn_2O_4$ possessed the highest k_{sapp} value.

3.4 Effect of temperature

The effect of reaction temperature (25, 35, 45 and 55 °C) on ENR removal in the process of PMS activation was studied. As displayed in Fig. 7(a–d), the ENR degradation in four Co_3O_4-composite spinels/PMS systems presented the similar trend, catalytic performances of Co_3O_4-composite spinels significantly increased with the increase of reaction temperature. As reaction temperature increased from 25 to 55 °C, k_{app} values of Co_3O_4–$CoFe_2O_4$, Co_3O_4–$CoMn_2O_4$, Co_3O_4–$CuCo_2O_4$ and Co_3O_4–$NiCo_2O_4$ increased from 0.122, 0.255, 0.273, 0.097 min^{-1} to 0.496, 0.872, 0.898, 0.498 min^{-1}, respectively. This result may be due to the fact that higher reaction temperature simplified the rupture of O–O bond and generation of $SO_4^{-\bullet}$.[29,30] In addition, higher reaction temperature was beneficial for reactant molecules to overcome activation energy barrier.[17] The activation energy (E_a) could be determined by plotting ln k_{app} against 1/T based on Arrhenius equation (Fig. 7(e)). The obtained E_a values were 40.73, 33.85, 33.07 and 45.51 kJ mol^{-1} in Co_3O_4–$CoFe_2O_4$, Co_3O_4–$CoMn_2O_4$, Co_3O_4–$CuCo_2O_4$ and Co_3O_4–$NiCo_2O_4$ activated PMS systems, respectively. The lower E_a value signified the higher catalytic reactivity, and the order of E_a was well corresponded to the sequence of catalytic activity. Moreover, all the E_a values were much higher than that of the diffusion-controlled reactions, which usually ranged from 10 to 13 kJ mol^{-1}.[31] This implied that the apparent reaction rate for

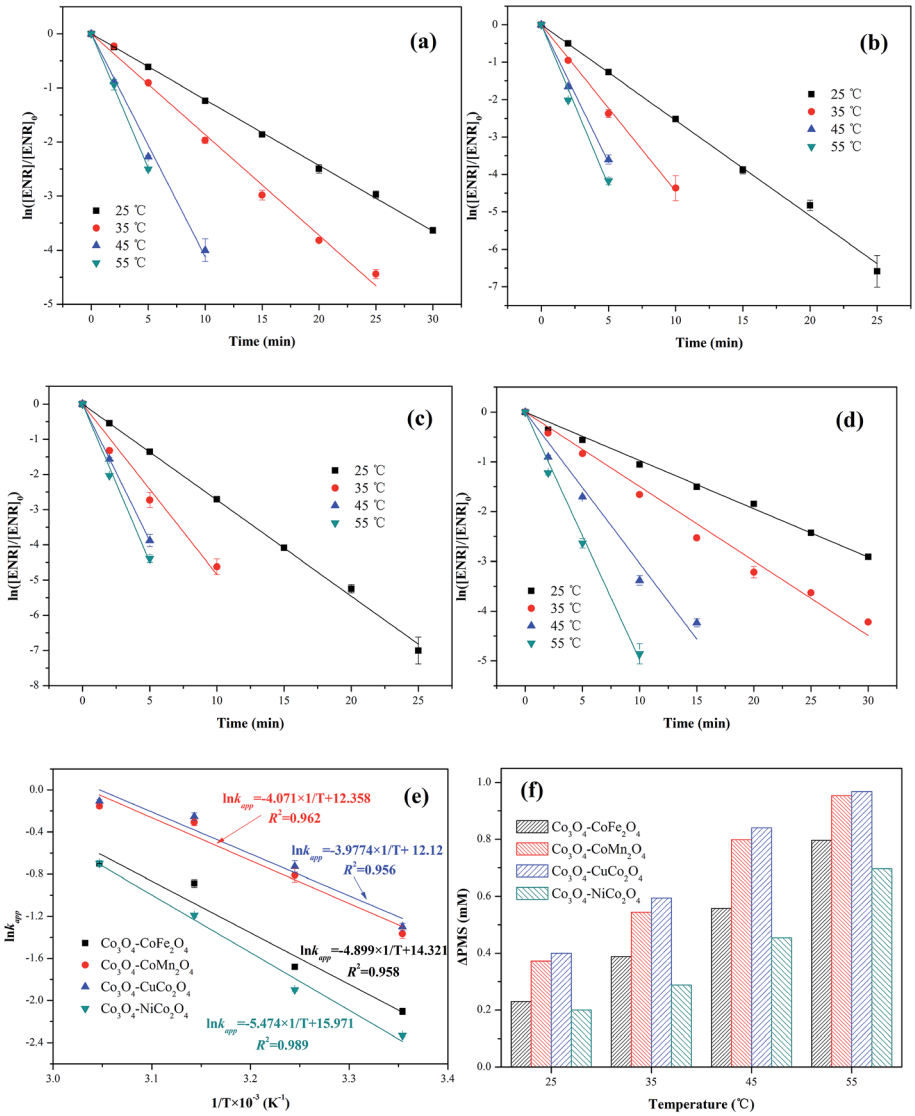

Fig. 7 Effect of reaction temperature on ENR degradation in different Co_3O_4-composite spinels/PMS systems: (a) Co_3O_4–$CoFe_2O_4$; (b) Co_3O_4–$CoMn_2O_4$; (c) Co_3O_4–$CuCo_2O_4$; (d) Co_3O_4–$NiCo_2O_4$. Parameters involved in different reaction temperatures and Co_3O_4-composite spinels/PMS systems: (e) Arrhenius curves; (f) ΔPMS. Experimental condition: [ENR] = 10 mg L^{-1}, [catalyst] = 0.1 g L^{-1}, [PMS] = 1 mM, pH_0 = 6.

ENR removal during Co_3O_4-composite spinels activated PMS processes was dominated by the rate of intrinsic chemical reactions on the catalyst surface. It was reported that out-sphere interactions were usually diffusion-controlled reactions, thus PMS activation by Co_3O_4-composite spinels was most likely an inner-sphere electron-transfer process.[32] The consumption of PMS during ENR oxidation processes was monitored (Fig. 7(f)). Similar with the trend of k_{app}, PMS consumption also increased as the reaction temperature increased. The PMS consumption caused by Co_3O_4–$CoFe_2O_4$, Co_3O_4–$CoMn_2O_4$, Co_3O_4–$CuCo_2O_4$ and Co_3O_4–$NiCo_2O_4$ increased from 0.230, 0.372, 0.400 and 0.200 mM to 0.796, 0.954, 0.968 and 0.696 mM with the reaction temperature increased from 25 to 55 °C, suggesting that higher reaction temperature was conducive to PMS activation and ENR degradation, which was well correspond to the conclusions by the observations of k_{app} values. In addition, the higher PMS consumption also reflected higher catalytic reactivity. From Fig. 7(f), the PMS consumption caused by Co_3O_4-composite spinels always showed the sequence of Co_3O_4–$CuCo_2O_4$ > Co_3O_4–$CoMn_2O_4$ > Co_3O_4–$CoFe_2O_4$ > Co_3O_4–$NiCuFe_2O_4$ even in different reaction temperatures, indicating that Co_3O_4–$CuCo_2O_4$ possessed the highest catalytic activity among the four Co_3O_4-composite spinels.

3.5 Radical identification and catalytic mechanism

Three different scavengers, *tert*-butyl alcohol (TBA), ethanol (EtOH) and phenol were employed to identify the dominant radical species in Co_3O_4-composite spinels/PMS systems. TBA can rapidly react with $^{\cdot}OH$ ($k_{\cdot OH}$ = 3.8–7.6 × 10^8 M^{-1} s^{-1}) but has a much lower reactivity with $SO_4^{\cdot-}$ ($k_{SO_4^{\cdot-}}$ = 4–9.1 × 10^5 M^{-1} s^{-1}),[33] and EtOH is a well scavenger for $^{\cdot}OH$ and $SO_4^{\cdot-}$ ($k_{\cdot OH}$ = 1.2–2.8 × 10^9 M^{-1} s^{-1}, $k_{SO_4^{\cdot-}}$ = 1.6–7.7 × 10^7 M^{-1} s^{-1}).[34] Phenol

can also react with $^{\cdot}OH$ and $SO_4^{-\cdot}$ at a high rate ($k_{\cdot OH} = 6.6 \times 10^9$ M^{-1} s^{-1}, $k_{SO_4^{-\cdot}} = 8.8 \times 10^9$ M^{-1} s^{-1}).[35] In view of the difference in reaction rates, using TBA, EtOH and phenol as scavengers was a feasible program for the identification of primary active species.

As presented in Fig. 8(a–d), only a slight reduction of ENR removal could be obtained in the presence of 10 or 100 mM TBA, implying that $^{\cdot}OH$ was involved in Co_3O_4-composite spinels activated PMS processes. With the addition of 10 mM EtOH, the ENR degradation was significantly inhibited and the removal efficiencies in Co_3O_4–$CoFe_2O_4$, Co_3O_4–$CoMn_2O_4$, Co_3O_4–$CuCo_2O_4$ and Co_3O_4–$NiCo_2O_4$ activated PMS processes were decreased from 97.37%, 100%, 100%, 94.56% to 66.84%, 69.92%, 82.42%, 57.81%, respectively. More addition of EtOH (100 mM) would cause further reduction of ENR removal efficiency with 47.90%, 47.70% 53.96% and 40.43%, respectively. In order to further confirm the contribution of $SO_4^{-\cdot}$, 10 mM phenol was introduced into solutions which resulted in a more significant inhibition to ENR removal, less than 18% of ENR could be decomposed in the four Co_3O_4-composite spinels/PMS processes. The quenching tests clearly suggested that $SO_4^{-\cdot}$ was the primary reactive species during PMS activation by Co_3O_4 composite spinels and $^{\cdot}OH$ was also involved in these processes.

XPS analysis of Co_3O_4–$CoFe_2O_4$ before and after catalytic oxidation was also performed to illustrate the heterogeneous catalytic mechanism (Fig. 4). As shown in Fig. 4(a), before catalytic oxidation, the contents of Co^{2+} and Co^{3+} was determined to be 65.34% and 34.66%. After catalytic oxidation, the proportions of Co^{2+} and Co^{3+} were changed to 61.93% and 38.07%, respectively. The partial increase of Co^{3+} was ascribed to the electrons donating of Co^{2+} during the oxidation process. In the case of O 1s spectra (Fig. 4(b)), the content of O_{latt} decreased from 48.26% to 46.35%, and the proportion of O_{ads} increased from 51.74% to 53.65%. The increment of O_{ads} can be attributed to the generation of Co–OH or O_2 adsorbed on the surface of Co_3O_4–$CoFe_2O_4$. It has been reported that $\equiv Co^{2+} - {}^{-}OH$ was the critical species for the generation of radicals during the process of PMS activation.[36] Of note, the Fe $2p_{3/2}$ envelope could be deconvoluted into Fe^{2+} at 709.5 eV, which indicated that the redox reactions between Co and Fe were involved in the PMS activation.

Based on the results of quenching experiments and XPS analysis, the plausible mechanisms of Co_3O_4-composite spinels activated PMS were put forward. Taking Co_3O_4–$CoFe_2O_4$/PMS system as example, H_2O molecules were firstly physically absorbed on the part of $\equiv Co^{2+}$ sites to generate $\equiv Co^{2+}$–^{-}OH. Then, $\equiv Co^{2+} - {}^{-}OH$ would react with HSO_5^- to form $SO_4^{-\cdot}$ after introduction of PMS (eqn (5)), and could regenerate through the reaction between formed $\equiv Co^{3+} - {}^{-}OH$ species and HSO_5^- (eqn (6)). Similarly, $\equiv Fe^{3+}$ could also combine with dissociative adsorption of H_2O molecules to form $\equiv Fe^{3+}$–^{-}OH, which would transform to $\equiv Fe^{2+} - {}^{-}OH$ (eqn (7)) and generate $SO_4^{-\cdot}$ by reacting with HSO_5^- (eqn (8)). In addition, due to the standard redox potential of $\equiv Co^{3+}/\equiv Co^{2+}$ was 1.92 V,[8] while the standard redox potential of $\equiv Fe^{3+}/\equiv Fe^{2+}$ was 0.77 V,[37] the

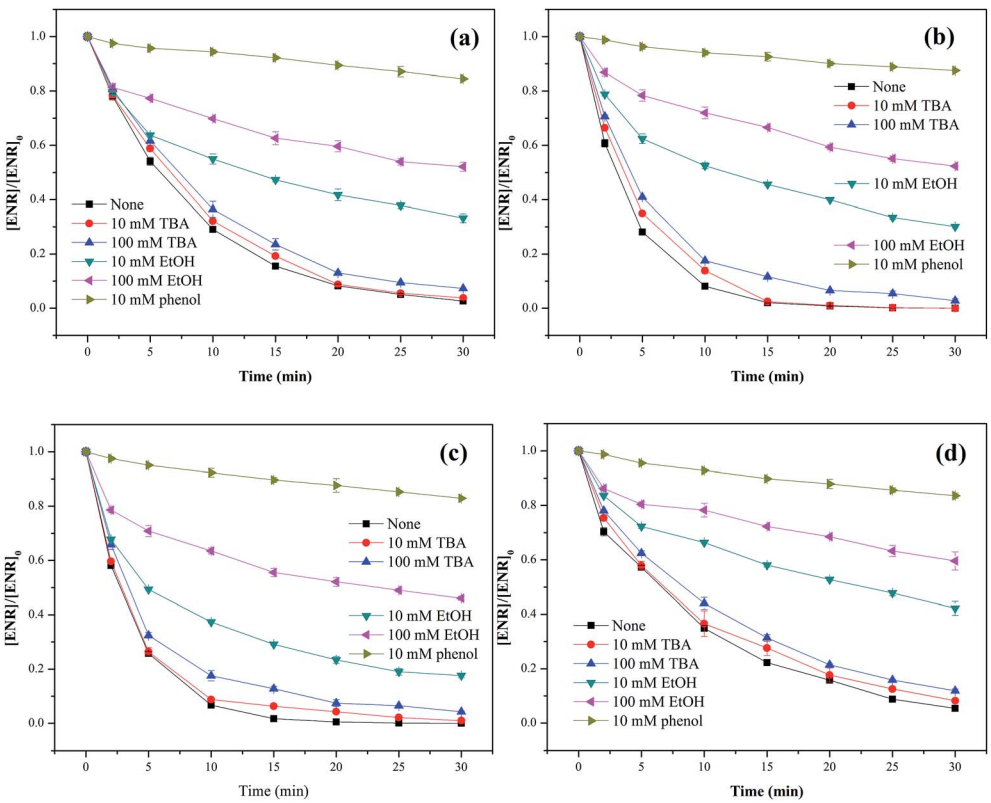

Fig. 8 Effect of quenchers on ENR degradation in different Co_3O_4-composite spinels/PMS systems: (a) Co_3O_4–$CoFe_2O_4$; (b) Co_3O_4–$CoMn_2O_4$; (c) Co_3O_4–$CuCo_2O_4$; (d) Co_3O_4–$NiCo_2O_4$. Experimental condition: [ENR] = 10 mg L^{-1}, [catalyst] = 0.1 g L^{-1}, [PMS] = 1 mM, $pH_0 = 6$, $T = 25$ °C.

reduction of $\equiv Co^{3+}$ by $\equiv Fe^{2+}$ was thermodynamically feasible (eqn (9)). The efficient regeneration of surface $\equiv Co^{2+}$ by this process may be able to remain the stability and high efficiency of Co_3O_4–$CoFe_2O_4$. Besides, $\equiv Co^{2+}$ or $\equiv Fe^{2+}$ on catalyst surface could also react with PMS to produce $^{\bullet}OH$ (eqn (10) and (11)), which could also be generate by the transformation of $SO_4^{-\bullet}$ (eqn (12) and (13)). Co_3O_4–$CoMn_2O_4$, Co_3O_4–$CuCo_2O_4$ and Co_3O_4–$NiCo_2O_4$ activated PMS processes all presented the similar mechanism with Co_3O_4–$CoFe_2O_4$ activated PMS process, and the reactions which were involved in Co_3O_4-composite spinels/PMS systems were listed in Table 2.

3.6 Reusability and stability of different Co_3O_4-composite spinels

The reusability of heterogeneous catalysts is an important indicator to assess the industrial application potential of heterogeneous catalysts. In this study, the reusability of different Co_3O_4-composite spinels was evaluated and the results were presented in Fig. 9(a). As shown, after being reused for three times, all the Co_3O_4-composite spinels still remained high catalytic activity toward PMS. Taking Co_3O_4–$CoFe_2O_4$ as example, after three consecutive runs, just a slight reduction in ENR removal was observed and their values were 94.89%, 91.32% and 89.27%, respectively. The slight loss of catalytic activity was mainly ascribed to the leaching of metal ions during the consecutive runs. Therefore, the stability of different Co_3O_4-composite spinels was further investigated and the results were reported in Fig. 9(b). As exhibited, the leaching of cobalt was clearly observed after each run. With the increase of cycle times, the leaching concentration decreased. Of note, after doped different transition metals into OM-Co_3O_4, the cobalt leakage can be effectively controlled, which was attributed to the intimate interactions between two metals.[2] Therefore, Co_3O_4-composite spinels are ideal PMS activator for environmental remediation.

Table 2 Reactions involved in composite spinels/PMS systems

Systems	Reactions	
Co_3O_4–$CoFe_2O_4$/PMS	$\equiv Co^{2+} - {}^{-}OH + HSO_5^{-} \rightarrow \equiv Co^{3+} - {}^{-}OH + SO_4^{-\bullet} + OH^{-}$	(5)
	$\equiv Co^{3+} - {}^{-}OH + HSO_5^{-} \rightarrow \equiv Co^{2+} - {}^{-}OH + SO_5^{-\bullet} + H^{+}$	(6)
	$\equiv Fe^{3+} - {}^{-}OH + HSO_5^{-} \rightarrow \equiv Fe^{2+} - {}^{-}OH + SO_5^{-\bullet} + H^{+}$	(7)
	$\equiv Fe^{2+} - {}^{-}OH + HSO_5^{-} \rightarrow \equiv Fe^{3+} - {}^{-}OH + SO_4^{-\bullet} + OH^{-}$	(8)
	$\equiv Fe^{2+} + \equiv Co^{3+} \rightarrow \equiv Fe^{3+} + \equiv Co^{2+}$	(9)
	$\equiv Co^{2+} + HSO_5^{-} \rightarrow \equiv Co^{3+} + SO_4^{2-} + {}^{\bullet}OH$	(10)
	$\equiv Fe^{2+} + HSO_5^{-} \rightarrow \equiv Fe^{3+} + SO_4^{2-} + {}^{\bullet}OH$	(11)
	$SO_4^{-\bullet} + H_2O \rightarrow HSO_4^{-} + {}^{\bullet}OH$	(12)
	$SO_4^{-\bullet} + OH^{-} \rightarrow SO_4^{2-} + {}^{\bullet}OH$	(13)
Co_3O_4–$CoMn_2O_4$/PMS	$\equiv Co^{2+} - {}^{-}OH + HSO_5^{-} \rightarrow \equiv Co^{3+} - {}^{-}OH + SO_4^{-\bullet} + OH^{-}$	
	$\equiv Co^{3+} - {}^{-}OH + HSO_5^{-} \rightarrow \equiv Co^{2+} - {}^{-}OH + SO_5^{-\bullet} + H^{+}$	
	$\equiv Mn^{3+} - {}^{-}OH + HSO_5^{-} \rightarrow \equiv Mn^{2+} - {}^{-}OH + SO_5^{-\bullet} + H^{+}$	
	$\equiv Mn^{3+} - {}^{-}OH + HSO_5^{-} \rightarrow \equiv Mn^{4+} - {}^{-}OH + SO_4^{-\bullet}$	
	$\equiv Mn^{2+} - {}^{-}OH + HSO_5^{-} \rightarrow \equiv Mn^{3+} - {}^{-}OH + SO_4^{-\bullet}$	
	$\equiv Mn^{4+} - {}^{-}OH + HSO_5^{-} \rightarrow \equiv Mn^{3+} - {}^{-}OH + SO_5^{-\bullet} + H^{+}$	
	$\equiv Mn^{2+} + \equiv Co^{3+} \rightarrow \equiv Mn^{3+} + \equiv Co^{2+}$	
	$\equiv Mn^{3+} + \equiv Co^{3+} \rightarrow \equiv Mn^{4+} + \equiv Co^{2+}$	
	$\equiv Co^{2+} + HSO_5^{-} \rightarrow \equiv Co^{3+} + SO_4^{2-} + {}^{\bullet}OH$	
	$\equiv Mn^{2+} + HSO_5^{-} \rightarrow \equiv Mn^{3+} + SO_4^{2-} + {}^{\bullet}OH$	
	$SO_4^{-\bullet} + H2O \rightarrow HSO_4^{-} + {}^{\bullet}OH$	
	$SO_4^{-\bullet} + OH^{-} \rightarrow SO_4^{2-} + {}^{\bullet}OH$	
Co_3O_4–$CuCo_2O_4$/PMS	$\equiv Co^{2+} - {}^{-}OH + HSO_5^{-} \rightarrow \equiv Co^{3+} - {}^{-}OH + SO_4^{-\bullet} + OH^{-}$	
	$\equiv Co^{3+} - {}^{-}OH + HSO_5^{-} \rightarrow \equiv Co^{2+} - {}^{-}OH + SO_5^{-\bullet} + H^{+}$	
	$\equiv Cu^{2+} - {}^{-}OH + HSO_5^{-} \rightarrow \equiv Cu^{+} - {}^{-}OH + SO_5^{-\bullet} + H^{+}$	
	$\equiv Cu^{2+} - {}^{-}OH + HSO_5^{-} \rightarrow \equiv Cu^{3+} - {}^{-}OH + SO_4^{-\bullet} + OH^{-}$	
	$\equiv Cu^{+} - {}^{-}OH + HSO_5^{-} \rightarrow \equiv Cu^{2+} - {}^{-}OH + SO_4^{-\bullet} + OH^{-}$	
	$\equiv Cu^{3+} - {}^{-}OH + HSO_5^{-} \rightarrow \equiv Cu^{2+} - {}^{-}OH + SO_5^{-\bullet} + H^{+}$	
	$\equiv Cu^{3+} + \equiv Co^{2+} \rightarrow \equiv Cu^{2+} + \equiv Co^{3+}$	
	$\equiv Cu^{+} + \equiv Co^{3+} \rightarrow \equiv Cu^{2+} + \equiv Co^{2+}$	
	$\equiv Co^{2+} + HSO_5^{-} \rightarrow \equiv Co^{3+} + SO_4^{2-} + {}^{\bullet}OH$	
	$\equiv Cu^{2+} + HSO_5^{-} \rightarrow \equiv {}^{3+} + SO_4^{2-} + {}^{\bullet}OH$	
	$SO_4^{-\bullet} + H_2O \rightarrow HSO_4^{-} + {}^{\bullet}OH$	
	$SO_4^{-\bullet} + OH^{-} \rightarrow SO_4^{2-} + {}^{\bullet}OH$	
Co_3O_4–$NiCo_2O_4$/PMS	$\equiv Co^{2+} - {}^{-}OH + HSO_5^{-} \rightarrow \equiv Co^{3+} - {}^{-}OH + SO_4^{-\bullet} + OH^{-}$	
	$\equiv Co^{3+} - {}^{-}OH + HSO_5^{-} \rightarrow \equiv Co^{2+} - {}^{-}OH + SO_5^{-\bullet} + H^{+}$	
	$\equiv Ni^{2+} - {}^{-}OH + HSO_5^{-} \rightarrow \equiv Ni^{3+} - {}^{-}OH + SO_4^{-\bullet} + OH^{-}$	
	$\equiv Ni^{3+} - {}^{-}OH + HSO_5^{-} \rightarrow \equiv Ni^{2+} - {}^{-}OH + SO_5^{-\bullet} + H^{+}$	
	$\equiv Co^{2+} + HSO_5^{-} \rightarrow \equiv Co^{3+} + SO_4^{2-} + {}^{\bullet}OH$	
	$\equiv Ni^{2+} + HSO_5^{-} \rightarrow \equiv Ni^{3+} + SO_4^{2-} + {}^{\bullet}OH$	
	$SO_4^{-\bullet} + H_2O \rightarrow HSO_4^{-} + {}^{\bullet}OH$	
	$SO_4^{-\bullet} + OH^{-} \rightarrow SO_4^{2-} + {}^{\bullet}OH$	

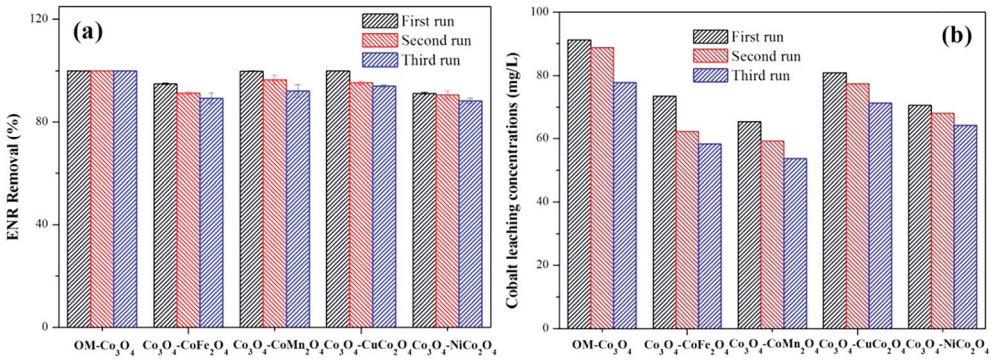

Fig. 9 (a) Reusability of different Co_3O_4-composite spinels as catalyst for the degradation of ENR; (b) cobalt leaching concentrations in different Co_3O_4-composite spinels/PMS systems. Experimental condition: [ENR] = 10 mg L^{-1}, [catalyst] = 0.1 g L^{-1}, [PMS] = 1 mM, pH_0 = 6, T = 25 °C, reaction time = 25 min.

4. Conclusion

Co_3O_4-composite spinels were successfully synthesized through doping transition metals (Fe, Mn, Cu and Ni) to ordered mesoporous Co_3O_4. The obtained Co_3O_4-composite spinels all showed outstanding catalytic activity toward PMS. Co_3O_4–$CuCo_2O_4$ exhibited the highest catalytic performance in PMS solution, followed by Co_3O_4–$CoMn_2O_4$, Co_3O_4–$CoFe_2O_4$ and Co_3O_4–$NiCo_2O_4$. ENR degradation would be retarded in strong acidic and alkaline conditions, the improvement of reaction temperature could significantly accelerate ENR decomposition. Sulfate radical was confirmed to be the primary reactive species in Co_3O_4-composite spinels activated PMS processes and hydroxyl radical was also involved in these processes. The synergistic effect between two metals in Co_3O_4-composite spinels was the vital reason for the high catalytic reactivity. Co_3O_4-composite spinels displayed satisfactory reusability and doping different transition metals into OM-Co_3O_4 can effectively control the cobalt leaching. In consideration of cost and toxicity, Co_3O_4-composite spinels might have great potential in pollution control than OM-Co_3O_4.

Conflicts of interest

No conflict of interest exists in the submission of this manuscript and manuscript is approved by all authors for publication.

Acknowledgements

The authors are grateful for the financial support of this study by the National Natural Science Foundation of China (No. 51508509), China Postdoctoral Science Foundation (No. 2015M581936), Natural Science Foundation of Zhejiang Province (No. LY18E080036) and State Key Laboratory of Pollution Control and Resource Reuse Foundation (No. PCRRF16017).

References

1 J. Zhou, J. Ma, L. W. Chen, X. C. Li, Y. H. Guan, P. C. Xie and C. Pan, *Environ. Sci. Technol.*, 2013, **47**, 11685–11691.
2 P. D. Hu and M. C. Long, *Appl. Catal., B*, 2016, **181**, 103–117.
3 Y. B. Wang, X. Zhao, D. Cao, Y. Wang and Y. F. Zhu, *Appl. Catal., B*, 2017, **211**, 79–88.
4 Y. M. Ren, L. Q. Lin, J. Ma, J. Yang, J. Feng and Z. J. Fan, *Appl. Catal., B*, 2015, **165**, 572–578.
5 C. Q. Tan, N. Y. Gao, D. F. Fu, J. Deng and L. Deng, *Sep. Purif. Technol.*, 2017, **175**, 47–57.
6 C. Q. Tan, D. F. Fu, N. Y. Gao, Q. D. Qin, Y. Xu and H. M. Xiang, *J. Photochem. Photobiol., A*, 2017, **332**, 406–412.
7 C. Q. Tan, Y. J. Dong, D. F. Fu, N. Y. Gao, J. X. Ma and X. Y. Liu, *Chem. Eng. J.*, 2018, **334**, 1006–1015.
8 G. P. Anipsitakis and D. D. Dionysiou, *Environ. Sci. Technol.*, 2004, **38**, 3705–3712.
9 G. P. Anipsitakis, E. Stathatos and D. D. Dionysiou, *J. Phys. Chem. B*, 2005, **109**, 13052–13055.
10 X. Y. Chen, J. W. Chen, X. L. Qiao, D. G. Wang and X. Y. Cai, *Appl. Catal., B*, 2008, **80**, 116–121.
11 J. Y. Pu, J. Q. Wan, Y. Wang and Y. W. Ma, *RSC Adv.*, 2016, **6**, 91791–91797.
12 S. N. Su, W. L. Guo, Y. Q. Leng, C. L. Yi and Z. M. Ma, *J. Hazard. Mater.*, 2013, **244–245**, 736–742.
13 J. Deng, Y. S. Shao, N. Y. Gao, C. Q. Tan, S. Q. Zhou and X. H. Hu, *J. Hazard. Mater.*, 2013, **262**, 836–844.
14 Y. J. Yao, Y. M. Cai, G. D. Wu, F. Y. Wei, X. Y. Li, H. Chen and S. B. Wang, *J. Hazard. Mater.*, 2015, **296**, 128–137.
15 Y. Feng, J. H. Liu, D. L. Wu, Z. Y. Zhou, Y. Deng, T. Zhang and K. M. Shih, *Chem. Eng. J.*, 2015, **280**, 514–524.
16 J. Deng, S. F. Feng, K. J. Zhang, J. Li, H. Y. Wang, T. Q. Zhang and X. Y. Ma, *Chem. Eng. J.*, 2017, **308**, 505–515.
17 R. C. Wei, F. Ge, M. Chen and R. Wang, *J. Environ. Qual.*, 2012, **41**, 1481–1486.
18 S. Waclawek, K. Grubel and M. Cernik, *Spectrochim. Acta, Part A*, 2015, **149**, 928–933.
19 T. Grewe, X. H. Deng, C. Weidenthaler, F. Schuth and H. Tuysuz, *Chem. Mater.*, 2013, **25**, 4926–4935.
20 J. Wu, Y. Xue, X. Yan, W. S. Yan, Q. M. Cheng and Y. Xie, *Nano Res.*, 2012, **5**, 521–530.
21 F. Ghanbari and M. Moradi, *Chem. Eng. J.*, 2017, **310**, 41–62.
22 R. A. Floyd and L. M. Soong, *Biochem. Biophys. Res. Commun.*, 1977, **74**, 79–84.

23 S. V. Verstraeten, S. Lucangioli and M. Galleano, *Inorg. Chim. Acta*, 2009, **362**, 2305–2310.
24 X. L. Zhang, M. B. Feng, L. S. Wang, R. J. Qu and Z. Y. Wang, *Chem. Eng. J.*, 2017, **307**, 95–104.
25 J. Deng, S. F. Feng, X. Y. Ma, C. Q. Tan, H. Y. Wang, S. Q. Zhou, T. Q. Zhang and J. Li, *Sep. Purif. Technol.*, 2016, **167**, 181–189.
26 C. Q. Tan, N. Y. Gao, Y. Deng, J. Deng and S. Q. Zhou, *J. Hazard. Mater.*, 2014, **276**, 452–460.
27 W. D. Oh, Z. L. Dong, Z. T. Hu and T. T. Lim, *J. Mater. Chem. A*, 2015, **3**, 22208–22217.
28 Y. Feng, P. H. Lee, D. Wu and K. Shih, *Water Res.*, 2017, **120**, 12–21.
29 P. H. Shi, R. J. Su, S. B. Zhu, M. C. Zhu, D. X. Li and S. H. Xu, *J. Hazard. Mater.*, 2012, **229–230**, 331–339.
30 J. Deng, Y. J. Ge, C. Q. Tan, H. Y. Wang, Q. S. Li, S. Q. Zhou and K. J. Zhang, *Chem. Eng. J.*, 2017, **330**, 1390–1400.
31 L. J. Xu and J. L. Wang, *Environ. Sci. Technol.*, 2012, **46**, 10145–10153.
32 Y. Feng, D. L. Wu, Y. Deng, T. Zhang and K. Shih, *Environ. Sci. Technol.*, 2016, **50**, 3119–3127.
33 Z. F. Huang, H. W. Bao, Y. Y. Yao, W. Y. Lu and W. X. Chen, *Appl. Catal., B*, 2014, **154–155**, 36–43.
34 Y. B. Deng, L. H. Zhu, N. Wang and H. Q. Tang, *Appl. Catal., B*, 2013, **129**, 153–162.
35 M. E. Lindsey and M. A. Tarr, *Environ. Sci. Technol.*, 2000, **34**, 444–449.
36 H. M. Sun, X. J. Yang, L. J. Zhao, T. H. Xu and J. S. Lian, *J. Mater. Chem. A*, 2016, **4**, 9455–9465.
37 Y. L. Nie, C. Hu, J. H. Qu and X. Zhao, *Appl. Catal., B*, 2009, **87**, 30–36.